Wang, S., Brown, M., Wang, L., Johnson, T.E., Olierook, H.K.H., Kirkland, C.L., Kylander-Clark, A., Evans, N.J., and McDonald, B.J., 2022, Two-stage exhumation of deeply subducted continental crust: Insight from zircon, titanite, and apatite petrochronology, Sulu belt of eastern China: GSA Bulletin, https://doi.org/10.1130/B36309.1.

Supplemental Material

Text. Analytical Methods.

Figure S1. Mineral maps made using a Tescan Integrated Mineral Analyzer of leucogranite sample (YK173-10a; A, B) and phengite gneiss sample (YK173-10b; C, D) to determine the mineral assemblage and modes (key at the bottom of the figure). Minerals abbreviated according to Whitney and Evans (2010).

Figure S2. Chondrite-normalized rare earth element patterns for zircon from three leucogranites (A–C) and three phengite gneisses (D–F).

Figure S3. Histograms of ^{207}Pb-corrected ^{238}U/^{206}Pb apparent ages for all titanites with F207% <80% (A) and F207% <90% (B) from the leucogranites and phengite gneisses.

Figure S4. Chondrite-normalized rare earth element patterns for titanite from three leucogranites (A–C) and three phengite gneisses (D–F).

Figure S5. Chondrite-normalized rare earth element patterns for apatite from three leucogranites (A–C) and three phengite gneisses (D–F).

Figure S6. Box-and-whisker plots summarizing pressure for three phengite gneisses calculated at *T* of 800 °C.

Figure S7. Box-and-whisker plots summarizing temperatures calculated at *P* of 2.9 GPa for mantles of zircon from three phengite gneisses (A) and at a notional *P* of 2.0 GPa for mantles/rims of zircon from three leucogranites and rims of zircon from the phengite gneisses (B).

Figure S8. Box-and-whisker plots summarizing temperatures calculated at a notional *P* of 1.2 GPa for rims of titanite from three leucogranites and three phengite gneisses.

Figure S9. A binary plot of $(Yb/Gd)_N$ versus Eu/Eu* for rims of titanite from three leucogranites and three phengite gneisses.

Table S1. Major element compositions of minerals in the leucogranites and phengite gneisses.

Table S2. Whole-rock major- and trace-element compositions of the leucogranites and phengite gneisses. Unit is wt% for major elements and ppm for trace elements, respectively.

Table S3. U–Pb isotope compositions of zircon from the leucogranites and phengite gneisses.

Table S4. Trace-element compositions (ppm) of zircon from the leucogranites and phengite gneisses.

Table S5. U–Pb isotope compositions of titanite from the leucogranites and phengite gneisses, together with the results for U–Pb reference materials.

Table S6. Trace-element compositions of titanite from the leucogranites and phengite gneisses, together with the results for reference materials.

Table S7. U–Pb isotope compositions of apatite from the leucogranites and phengite gneisses, together with the results for U–Pb reference materials.

Table S8. Trace-element compositions of apatite from the leucogranites and phengite gneisses, together with the results for reference materials.

Table S9. Whole-rock Sr and Nd isotope compositions of the leucogranites and phengite gneisses.

ANALYTICAL METHODS

Compositional Mapping

Mineral identification and determination of modes was conducted on carbon-coated thin sections using a Tescan Integrated Mineral Analyzer housed at Nanjing Hongchuang Geological Exploration Technology Service Co., Ltd. The data were collected in 'dot mapping' mode that includes simultaneous collection of back-scattered electron (BSE) and energy dispersive spectrometry (EDS) data. At each point, the BSE level is determined (i.e., to distinguish minerals from the epoxy based on different BSE signal). If the BSE level is at a certain threshold of 15–100, the beam is held in place until 1000 counts from the spectrometer are collected. The working conditions included an accelerating voltage of 25 kV, probe current of 9 nA and working distance of 15 mm. Pixel spacing was set to 3 μm and dot spacing was set to 9 μm. The current and BSE signal intensity were calibrated on a platinum Faraday cup using an automated procedure. EDS performance was checked using a manganese standard.

Mineral Major Element Analysis

Major element compositions were acquired on polished thin sections using a JEOL JXA-8230 electron microprobe analyzer (EPMA) with four wavelength-dispersive spectrometers at the Center for Global Tectonics in the School of Earth Sciences, China University of Geosciences, Wuhan. The operating conditions were 15 kV accelerating voltage, 20 nA probe current, and 1 μm beam diameter. Dwell times were 10s on element peaks and 5s on background. Raw X-ray intensities were corrected using a ZAF procedure. A series of natural and synthetic standards from Structure Probe, Inc. Company was utilized, including: sanidine (K), pyrope garnet (Fe, Al), diopside (Ca, Mg), jadeite (Na), rhodonite (Mn), olivine (Si) and rutile (Ti).

Whole-rock Geochemistry

Unweathered rock samples were broken into pieces and processed to <60 mesh in a corundum jaw crusher. For each sample, ~70 g was further powdered in an agate ring mill to <200 mesh for whole-rock major oxide, trace element and Sr–Nd isotope analyses. Whole-rock

major element compositions were acquired using conventional X-ray fluorescence (XRF, Primus II, Rigaku, Japan) at the Wuhan Sample Solution Analytical Technology Co. Ltd., Wuhan, China. The details of sample-digestion procedure were as follows: (1) Sample powder was placed in an oven at 105 ºC to dry for 12 h; (2) ~1.0 g of the dried sample was accurately weighted and placed in a ceramic crucible, and then heated in a muffle furnace at 1000 ºC for 2 h. After cooling to 400 ºC, the sample was placed in a drying vessel and weighted again to calculate the loss on ignition (LOI); (3) 0.6 g sample powder was mixed with 6.0 g cosolvent ($Li_2B_4O_7$:$LiBO_2$:LiF = 9:2:1) and 0.3 g oxidant (NH_4NO_3) in a Pt crucible, which was placed in a furnace at 1150 ºC for 14 min. Then, the molten sample was quenched in air for 1 min to produce flat discs on a fire brick for analysis. The analytical uncertainty is generally <5%.

Trace element concentrations were analyzed using an Agilent 7500e ICP-MS (inductively coupled plasma mass spectrometry) at the Wuhan Sample Solution Analytical Technology Co. Ltd., Wuhan, China. International standards, including AGV-2, BHVO-2, BCR-2 and RGM-2, were used as reference materials. The detailed sample digestion procedure for ICP-MS analysis, and the analytical precision and accuracy for trace elements are similar to those described by Liu et al. (2008).

Sr and Nd isotope analysis of samples was performed on a Neptune Plus MC (multi-collector)-ICP-MS (Thermo Fisher Scientific, Dreieich, Germany) at the Wuhan Sample Solution Analytical Technology Co., Ltd., Wuhan, China. The Neptune Plus, a double focusing MC–ICP–MS, was equipped with seven fixed electron multiplier ICs, and nine Faraday cups fitted with 10^{11} Ω resistors. The large dry interface pump (120 m^3 hr^{-1} pumping speed) and newly designed X skimmer cone and Jet sample cone were used to increase instrumental sensitivity. Sr and Nd single element solutions from Alfa (Alfa Aesar, Karlsruhe, Germany) were used to optimize instrument operating parameters. Aliquots of the international standard solutions of 200 μg L^{-1} NIST SRM 987 and JNdi-1 were used regularly for evaluating the reproducibility and accuracy of the instrument. Typically, the signal intensities of ^{88}Sr in NIST SRM 987 and ^{144}Nd+ in JNdi-1 were >~4.0 V and >~2.5 V, respectively. The Sr and Nd isotopic data were acquired in the static mode at low resolution. The routine data acquisition consisted of ten blocks of 10 cycles (4.194 s integration time per cycle).

The exponential law, which initially was developed for TIMS measurement (Russell et al., 1978) and remains the most widely accepted and utilized with MC-ICP-MS, was used to assess the instrumental mass discrimination in this study. Mass discrimination correction was carried out via internal normalization to $^{88}Sr/^{86}Sr = 8.375209$ and $^{146}Nd/^{144}Nd = 0.7219$ (Lin et al., 2016). During the measurement, analyses of the NIST SRM 987 standard yielded an average $^{87}Sr/^{86}Sr$ ratio of 0.710244 ± 22 (2SD, n = 32), and the JNdi-1 standard gave an average $^{143}Nd/^{144}Nd$ ratio of 0.512118 ± 15 (2SD, n = 31), which are identical within error to their published values (0.710241 ± 12 and 0.512115 ± 07, respectively; Thirlwall, 1991; Tanaka et al., 2000). In addition, the USGS reference materials BCR-2 (basalt) and RGM-2 (rhyolite) yielded results of 0.705034 ± 14 (2SD, n = 4) and 0.704192 ± 10 (2SD, n = 4) for $^{87}Sr/^{86}Sr$, and 0.512644 ± 15 (2SD, n = 6) and 0.512810 ± 15 (2SD, n = 4) for $^{143}Nd/^{144}Nd$, respectively, which are also consistent within error with published values (Li et al., 2012).

Cathodoluminescence (CL) and BSE Imaging

Zircon, titanite and apatite grains were separated from three leucogranite (YK173-10a, YK1711-11a and YK192-1a) and three phengite gneiss (YK173-10b, YK1711-11b and YK192-

1b) samples following standard crushing, sieving, heavy liquid and magnetic separation techniques. Individual zircon, titanite and apatite grains for analysis were further separated from any remaining contaminants using a binocular microscope. For each sample, a portion of all three mineral separates was mounted in a 24 mm diameter epoxy resin block, respectively, and polished to about half thickness for U–Pb isotope and trace-element analyses. CL images for the zircon mounts and BSE images for the titanite and apatite mounts were acquired using a FEI Quanta 450 field emission gun scanning electron microscope equipped with a Gatan Mono CL4+ CL system at the State Key Laboratory of Geological Processes and Mineral Resources, China University of Geosciences, Wuhan. The operating conditions for the CL imaging were an accelerating voltage of 10 kV, a spot size of 5 μm and a working distance of ~14 mm, and for the BSE imaging were an accelerating voltage of 20 kV and a spot size of 6 μm with a working distance of ~12 mm.

Zircon U–Pb Geochronology and Trace Elements

U–Pb isotope and trace-element analysis of zircon was determined at the University of California, Santa Barbara, following the methods outlined in Kylander-Clark et al. (2014). The laser-ablation split-stream system combines a Photon Machines 193 nm ArF Excimer laser, equipped with a Hel-Ex ablation cell, with a Nu Instruments HR Plasma high-resolution MC–ICP–MS system for collecting U–Pb isotope data, and an Agilent 7700 quadrupole for determining trace-element concentrations. The laser parameters for analysis consisted of a 10 μm spot ablated at ~1 j/cm^2 and 4 Hz for 15 seconds, following a 20 second baseline. Unknowns were bracketed by zircon reference material 91500 (Wiedenbeck et al., 1995); zircon reference material RMs GJ1 (Jackson et al., 2004), NIST612 and Plešovice (Sláma et al., 2008) were included occasionally for quality control. During the period of analysis, GJ1 and Plešovice yielded average ages within 1% of their accepted values. For analysis of trace-element concentrations, ^{90}Zr was used as the internal standard and 91500 (Liu et al., 2010) was used as the reference material; GJ1 yields concentrations consistent with accepted values (Liu et al., 2010). Raw U–Pb isotope and trace-element data were reduced using Iolite v3 (Paton et al., 2011) to correct for instrument drift, laser-ablation-induced down-hole elemental fractionation, plasma-induced elemental fractionation, and instrumental mass bias.

Titanite and Apatite U–Pb Geochronology and Trace Elements

Titanite and apatite U–Pb isotope and trace-element measurements were collected in the GeoHistory Facility, JdLC, Curtin University. An excimer laser (Resonetics S-155-LR 193 nm) was used with a spot size of 50 μm, an on-sample fluence of 2.4 J cm^{-2} (titanite) or 2.3 J cm^{-2} (apatite) and repetition rate of 5 Hz for ~35 s of total analysis time and 60 s of background capture. All analyses were preceded by three cleaning pulses. The sample cell was flushed by ultrahigh purity He (0.32 L min^{-1}) and N_2 (1.2 mL min^{-1}).

U–Pb data were collected on an Agilent 7700s quadrupole mass spectrometer with high purity Ar as the carrier gas for both sessions (flow rate 0.98 L min^{-1}). Analyses of ~20 unknowns were bracketed by analysis of a standard block containing the primary reference material, which was used to monitor and correct for mass fractionation and instrumental drift material, and secondary reference material(s) to monitor data accuracy and precision. For titanite, the primary reference material was MKED1 (1517.32 ± 0.32 Ma; Spandler et al., 2016) and BLR-1 (1047.1 ±

0.4 Ma; Aleinikoff et al., 2007) was employed as a secondary standard. During the analytical session, when reduced to MKED1, BLR-1 yielded a statistically-reliable (p >0.05) regressed age of 1042 ± 5 Ma (anchored to published $^{207}Pb/^{206}Pb_{(c)}$ = 0.912), which is within 2σ of the published age (see supplementary Table S3 for full compilation of results for U–Pb reference materials). For apatite, the primary reference material was Madagascar (474.25 ± 0.41 Ma; Thomson et al., 2012), with Mount McClure (523.5 ± 1.5 Ma; Schoene and Bowring, 2006) and AS3 (FC-Duluth; 1099.1 ± 1.2 Ma; Schmitz et al., 2003) as secondary standards. During the analytical session, when reduced to Madagascar, Mount McClure and AS3 yielded statistically-reliable (p >0.05) regressed ages (anchored to published $^{207}Pb/^{206}Pb$ intercepts) of 515 ± 15 and 1101 ± 41 Ma, respectively, both of which are within 2σ of the published age (see supplementary Table 5 for full compilation of results for U–Pb reference materials). U–Pb data were reduced using the VizualAge UComPbine data reduction scheme in Iolite4 (Chew et al., 2014; Paton et al., 2011) and in-house Excel macros. Concordia plots were constructed using Isoplot 4.15 software (Ludwig, 2012).

Trace-element compositions were determined from the same sample volume as U–Pb analyses. For titanite, 34 isotopes were measured (^{23}Na, ^{27}Al, ^{29}Si, ^{43}Ca, ^{47}Ti, ^{51}V, ^{52}Cr ^{55}Mn, ^{56}Fe, ^{89}Y, ^{91}Zr, ^{93}Nb, ^{139}La, ^{140}Ce, ^{141}Pr, ^{146}Nd, ^{147}Sm, ^{153}Eu, ^{157}Gd, ^{159}Tb, ^{163}Dy, ^{165}Ho, ^{166}Er, ^{169}Tm, ^{172}Yb, ^{175}Lu, ^{178}Hf, ^{181}Ta, ^{208}Pb, ^{232}Th and ^{238}U). For apatite, 26 isotopes were measured (^{24}Mg, ^{29}Si, ^{31}P, ^{43}Ca, ^{44}Ca, ^{51}V, ^{55}Mn, ^{88}Sr, ^{89}Y, ^{139}La, ^{140}Ce, ^{141}Pr, ^{146}Nd, ^{147}Sm, ^{153}Eu, ^{157}Gd, ^{159}Tb, ^{163}Dy, ^{165}Ho, ^{166}Er, ^{169}Tm, ^{172}Yb, ^{175}Lu, ^{208}Pb, ^{232}Th and ^{238}U). For both titanite and apatite, dwell time for most elements was 0.02 s, with Si and P monitored for 0.01 s. International glass standard NIST 610 was used as the primary reference material for calculation of concentrations and to correct for instrumental drift. For titanite, ^{29}Si was the internal standard, assuming stoichiometric 14.20% Si in titanite. For apatite, ^{43}Ca was the internal standard, assuming stoichiometric 39.36% Ca in apatite. During the time-resolved analysis, contamination resulting from inclusions and compositional zoning were monitored and only the relevant part of the signal was integrated. Secondary trace element standard NIST 612, treated as an unknown, reproduced recommended values to within 1% for most elements in both sessions. For titanite, exceptions were Tb (1.1%) and Ti (2.7%), and for apatite, Mg (4.3%) and P (2.9%) were in error. Trace element data were reduced in Iolite4 (Paton et al., 2011).

Ti-in-Zircon and Zr-in-Titanite Thermometry

Ti-in-zircon and Zr-in-titanite temperatures were calculated using the method of Ferry and Watson (2007) and Hayden et al. (2008), respectively. As quartz is a major phase within the studied rocks, a_{SiO2} was set as 1.0. However, rutile is not observed and titanite is the Ti-rich mineral in both the leucogranite and phengite gneiss; therefore, the activity of TiO_2 (a_{TiO2}) is lower than 1.0. Given the plausible limits of a_{TiO2} = 0.5–1.0 in typical crustal rocks (Ferry and Watson, 2007; Hayden and Watson, 2007), we used a_{TiO2} = 0.75. The resultant temperatures are summarized in box-and-whisker plots in Figs. S7 and S8, respectively.

Monte Carlo Simulations of Cooling and Exhumation Rates

To compute cooling and exhumation rates, we used Monte Carlo simulations to propagate uncertainties and minimize error correlations. The Monte Carlo simulations were performed in Excel, using the Excel add-on program QuantumXL by SigmaZone. The

probability distributions and values of variables are summarized in Table 4. Input probability distributions were expected to be Gaussian for all input data. Output rates are at 95% confidence. The Monte Carlo simulations were performed using 10,000 iterations. In each iteration, QuantumXL randomly selects a value for uncertain variables using a Mersenne Twister pseudo-random number generator, based on the user-defined probability distributions. These values are then used to calculate the cooling and exhumation rates. After 10,000 iterations, histograms of output values are generated, showing the distribution of computed rates. These histograms represent the probability distribution of the true range of the variables calculated using the Monte Carlo simulations.

REFERENCES CITED

Aleinikoff, J.N., Wintsch, R.P., Tollo, R.P., Unruh, D.M., Fanning, C.M., and Schmitz, M.D., 2007, Ages and origins of rocks of the Killingworth dome, south-central Connecticut: Implications for the tectonic evolution of southern New England: American Journal of Science, v. 307, no. 1, p. 63–118, https://doi.org/10.2475/01.2007.04.

Caddick, M.J., and Thompson, A.B., 2008, Quantifying the tectono-metamorphic evolution of pelitic rocks from a wide range of tectonic settings: mineral compositions in equilibrium: Contributions to Mineralogy and Petrology, v. 156, no. 2, p. 177–195, https://doi.org/10.1007/s00410-008-0280-6.

Chew, D.M., Petrus, J.A., and Kamber, B.S., 2014, U–Pb LA–ICPMS dating using accessory mineral standards with variable common Pb: Chemical Geology, v. 363, p. 185–199, https://doi.org/10.1016/j.chemgeo.2013.11.006.

Ferry, J.M., and Watson, E.B., 2007, New thermodynamic models and revised calibrations for the Ti-in-zircon and Zr-in-rutile thermometers: Contributions to Mineralogy and Petrology, v. 154, no. 4, p. 429–437, https://doi.org/10.1007/s00410-007-0201-0.

Hayden, L.A., and Watson, E.B., 2007, Rutile saturation in hydrous siliceous melts and its bearing on Ti-thermometry of quartz and zircon: Earth and Planetary Science Letters, v. 258, no. 3–4, p. 561–568, https://doi.org/10.1016/j.epsl.2007.04.020.

Hayden, L.A., Watson, E.B., and Wark, D.A., 2008, A thermobarometer for sphene (titanite): Contributions to Mineralogy and Petrology, v. 155, no. 4, p. 529–540, https://doi.org/10.1007/s00410-007-0256-y.

Jackson, S.E., Pearson, N.J., Griffin, W.L., and Belousova, E.A., 2004, The application of laser ablation-inductively coupled plasma-mass spectrometry to in situ U–Pb zircon geochronology: Chemical Geology, v. 211, no. 1–2, p. 47–69, https://doi.org/10.1016/j.chemgeo.2004.06.017.

Kylander-Clark, A.R., and Hacker, B.R., 2014, Age and significance of felsic dikes from the UHP western gneiss region: Tectonics, v. 33, no. 12, p. 2342–2360, https://doi.org/10.1002/2014TC003582.

Li, C.F., Li, X.H., Li, Q.L., Guo, J.H., and Yang, Y.H., 2012, Rapid and precise determination of Sr and Nd isotopic ratios in geological samples from the same filament loading by thermal ionization mass spectrometry employing a single-step separation scheme: Analytica Chimica Acta, v. 727, no. 10, p. 54–60, https://doi.org/10.1016/j.aca.2012.03.040.

Lin, J., Liu, Y.S., Yang, Y.H., and Hu, Z.C., 2016, Calibration and correction of LA-ICP-MS and LA-MC-ICP-MS analyses for element contents and isotopic ratios: Solid Earth Sciences, v. 1, p. 5–27, https://doi.org/10.1016/j.sesci.2016.04.002.

Liu, Y.S., Zong, K.Q., Kelemen, P.B., and Gao, S., 2008, Geochemistry and magmatic history of eclogites and ultramafic rocks from the Chinese continental scientific drill hole: subduction and ultrahigh-pressure metamorphism of lower crustal cumulates: Chemical Geology, v. 247, p. 133–153, https://doi.org/10.1016/j.chemgeo.2007.10.016.

Liu, Y.S., Gao, S., Hu, Z.C., Gao, C., Zong, K., and Wang, D., 2010, Continental and oceanic crust recycling-induced melt–peridotite interactions in the Trans-North China Orogen: U–Pb dating, Hf isotopes and trace elements in zircons from mantle xenoliths: Journal of Petrology, v. 51, p. 537–571, https://doi.org/10.1093/petrology/egp082.

Ludwig, K.R., 2012, User's manual for Isoplot 3.75. A Geochronological Toolkit for Microsoft Excel. Berkeley Geochronology Center Special Publication No. 5, 75 pp.

Paton, C., Hellstrom, J., Paul, B., Woodhead, J., and Hergt, J., 2011, Iolite: Freeware for the visualisation and processing of mass spectrometric data: Journal of Analytical Atomic Spectrometry, v. 26, p. 2508–2518 https://xs.scihub.ltd/10.1039/C1JA10172B, https://doi.org/10.1039/c1ja10172b.

Russell, W.A., Papanastassiou, D.A., Tombrello, T.A., 1978. Ca isotope fractionation on the earth and other solar system materials. Geochimica et Cosmochimica Acta, v. 42, no. 8, p. 1075–1090. https://doi.org/10.1016/0016-7037(78)90105-9.

Schoene, B., and Bowring, S.A., 2006, U–Pb systematics of the McClure Mountain syenite: thermochronological constraints on the age of the $^{40}Ar/^{39}Ar$ standard MMhb: Contributions to Mineralogy and Petrology, v. 151, no. 5, p. 615–630, https://doi.org/10.1007/s00410-006-0077-4.

Schmitz, M.D., Bowring, S.A., and Ireland, T.R., 2003, Evaluation of Duluth Complex anorthositic series (AS3) zircon as a U-Pb geochronological standard: New high-precision isotope dilution thermal ionization mass spectrometry results: Geochimica et Cosmochimica Acta, v. 67, no. 19, p. 3665–3672, https://doi.org/10.1016/S0016-7037(03)00200-X.

Sláma, J., Košler, J., Condon, D.J., Crowley, J.L., Gerdes, A., Hanchar, J.M., Horstwood, M.S.A., Morris, G.A., Nasdala, L., Norberg, N., Schaltegger, U., Schoene, B., Tubrett, M.N., and Whitehouse, M.J., 2008, Plešovice zircon—a new natural reference material for U–Pb and Hf isotopic microanalysis: Chemical Geology, v. 249, no. 1–2, p. 1–35, https://doi.org/10.1016/j.chemgeo.2007.11.005.

Spandler, C., Hammerli, J., Sha, P., Hilbert-Wolf, H., Hu, Y., Roberts, E., and Schmitz, M., 2016, MKED1: a new titanite standard for in situ analysis of Sm–Nd isotopes and U–Pb geochronology: Chemical Geology, v. 425, p. 110–126, https://doi.org/10.1016/j.chemgeo.2016.01.002.

Sun, S.S., and McDonough, W.F., 1989, Chemical and isotopic systematics of oceanic basalts: Implications for mantle composition and processes: Geological Society of London, Special Publications, v. 42, p. 313–345, https://doi.org/10.1144/GSL.SP.1989.042.01.19.

Tanaka, T., Togashi, S., Kamioka, H., Amakawa, H., Kagami, H., Hamamoto, T., et al., 2000, Jndi-1: a neodymium isotopic reference in consistency with lajolla neodymium: Chemical Geology, v. 168, p. 279–281, https://doi.org/10.1016/S0009-2541(00)00198-4.

Thirlwall, M.F., 1991, Long-term reproducibility of multicollector sr and nd isotope ratio analysis: Chemical Geology, v. 94, no. 2, p. 85–104, https://doi.org/10.1016/S0009-2541(10)80021-X.

Thomson S.N., Gehrels, G.E., Ruiz, J., and Buchwaldt, R., 2012, Routine low-damage U–Pb dating of apatite using laser ablation-multicollector-ICPMS: Geochemistry, Geophysics, Geosystems, v. 13, Q0AA21, https://doi.org/10.1029/2011GC003928.

Whitney, D.L., and Evans, B.W., 2010, Abbreviations for names of rock-forming minerals: The American Mineralogist, v. 95, no. 1, p. 185–187, https://doi.org/10.2138/am.2010.3371.
Wiedenbeck, M., Alle, P., Corfu, F., Griffin, W.L., Meier, M., Oberli, F., Quadt, A.V., Roddick, J.C., and Spiegel, W., 1995, Three natural zircon standards for U–Th–Pb, Lu–Hf, trace element and REE analyses: Geostandards Newsletter, v. 19, p. 1–23, https://doi.org/10.1111/j.1751-908X.1995.tb00147.x.
Xia, B., Brown, M., Wang, L., Wang, S.J., and Piccoli, P., 2018, Phase equilibria modeling of MT–UHP eclogite: a case study of coesite eclogite at Yangkou, Sulu belt, Eastern China: Journal of Petrology, v. 59, no. 7, p. 1253–1280, https://doi.org/10.1093/petrology/egy060.

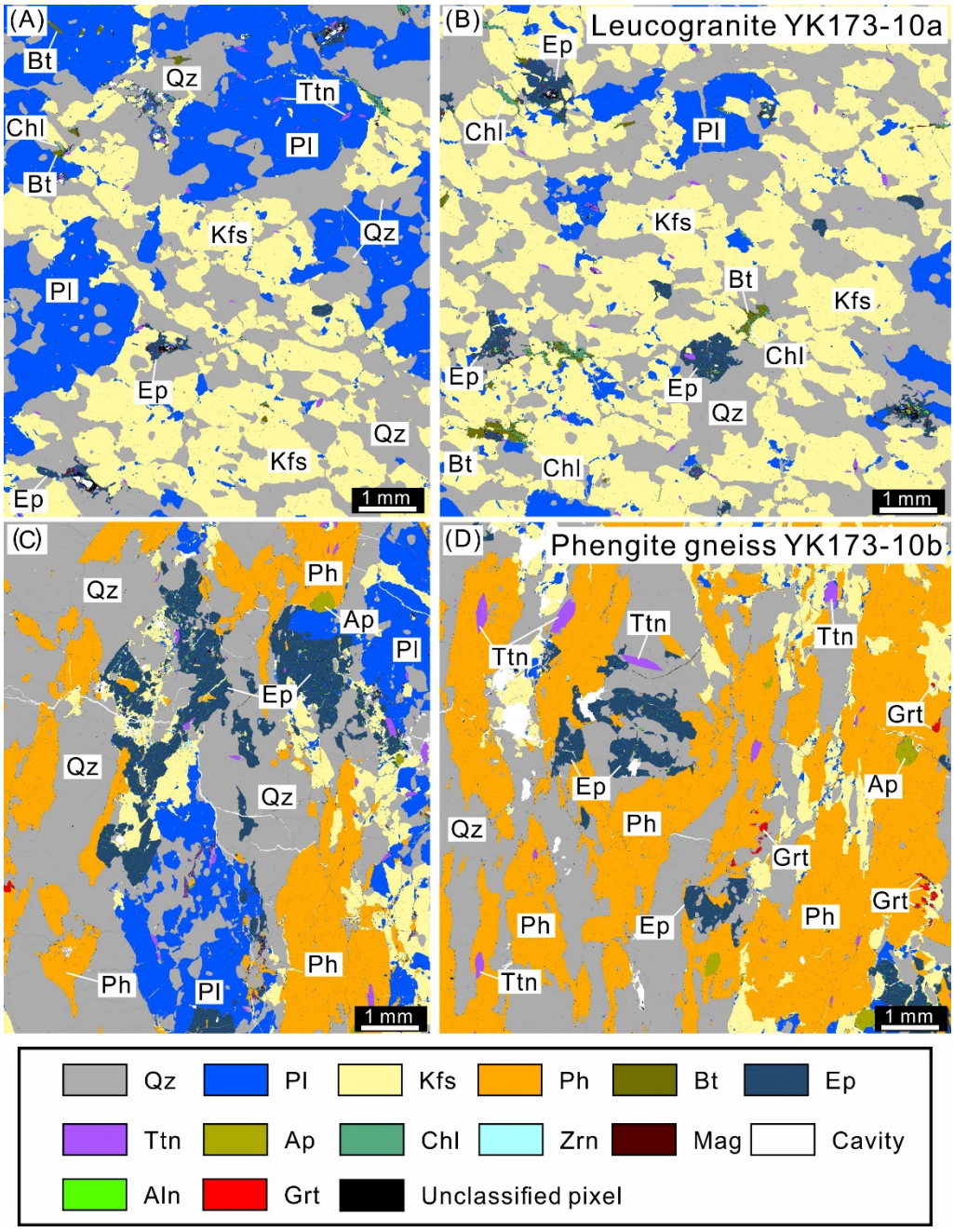

Figure S1. Mineral maps made using a Tescan Integrated Mineral Analyzer of leucogranite sample (YK173-10a; A, B) and phengite gneiss sample (YK173-10b; C, D) to determine the mineral assemblage and modes (key at the bottom of the figure). Minerals abbreviated according to Whitney and Evans (2010).

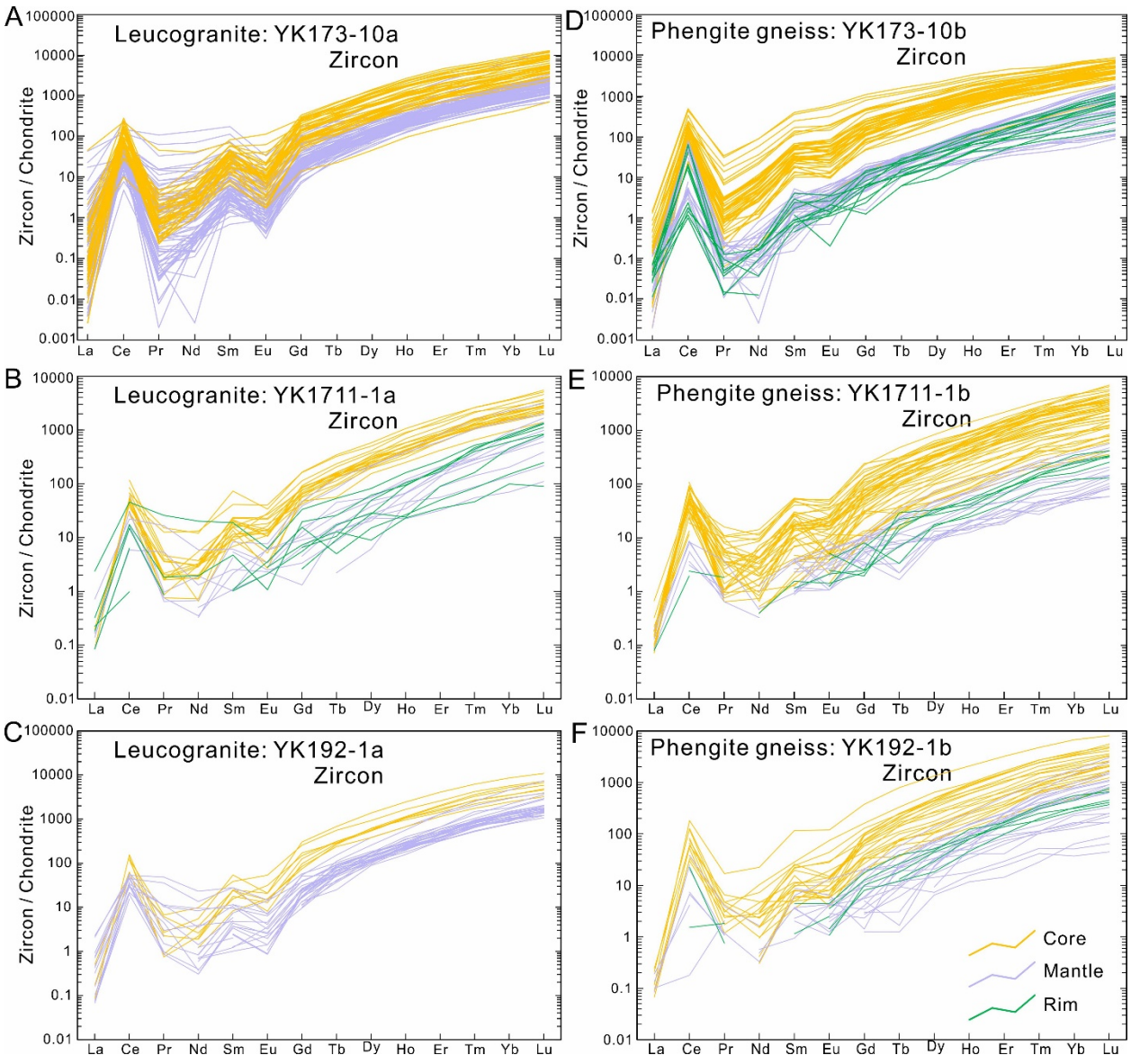

Figure S2. Chondrite-normalized rare earth element patterns for zircon from three leucogranites (A–C) and three phengite gneisses (D–F). Normalizing values are from Sun and McDonough (1989).

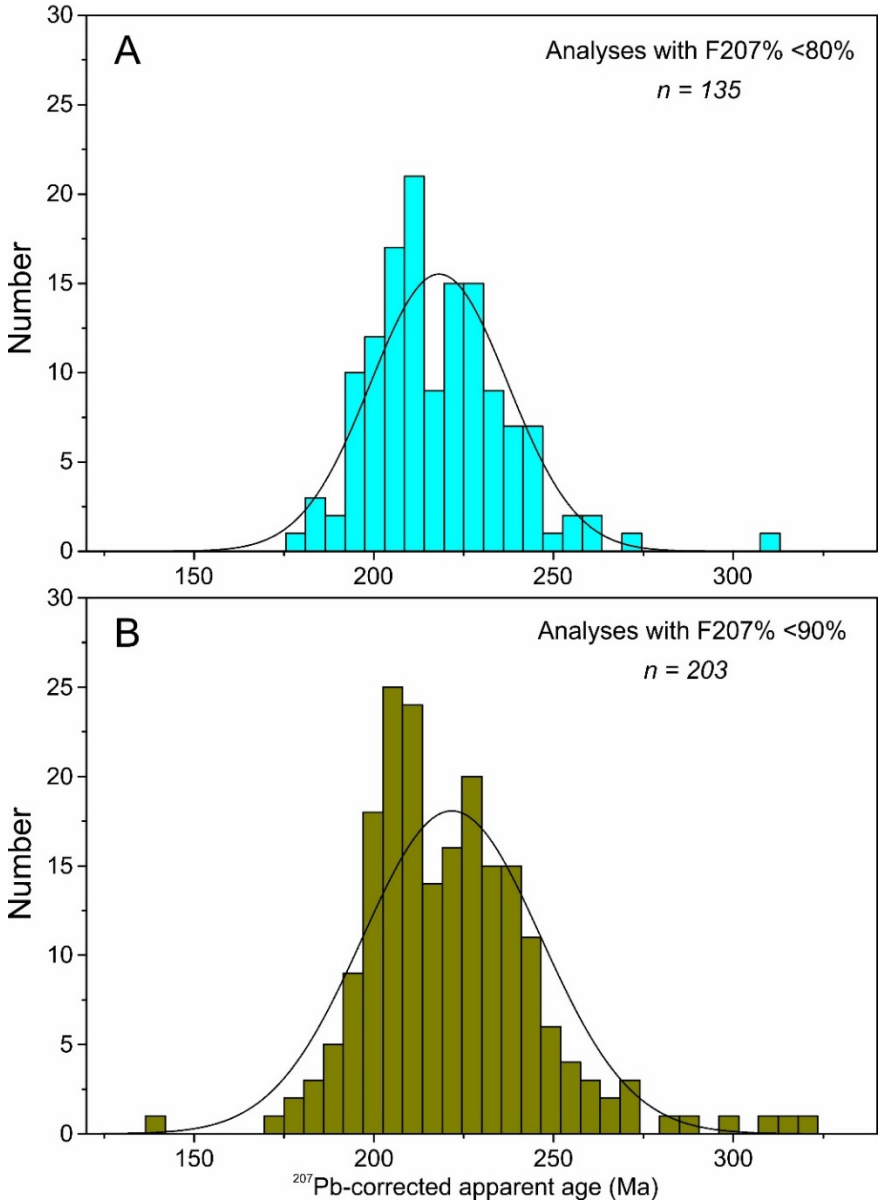

Figure S3. Histograms of ^{207}Pb-corrected ^{238}U/^{206}Pb apparent ages for all titanites with F207% <80% (A) and F207% <90% (B) from the leucogranites and phengite gneisses. The common Pb value to calculate the ages is 0.9205. F207% is the distance upwards along a mixing line towards common Pb from radiogenic Pb where 100% represents an analysis dominated by the common component.

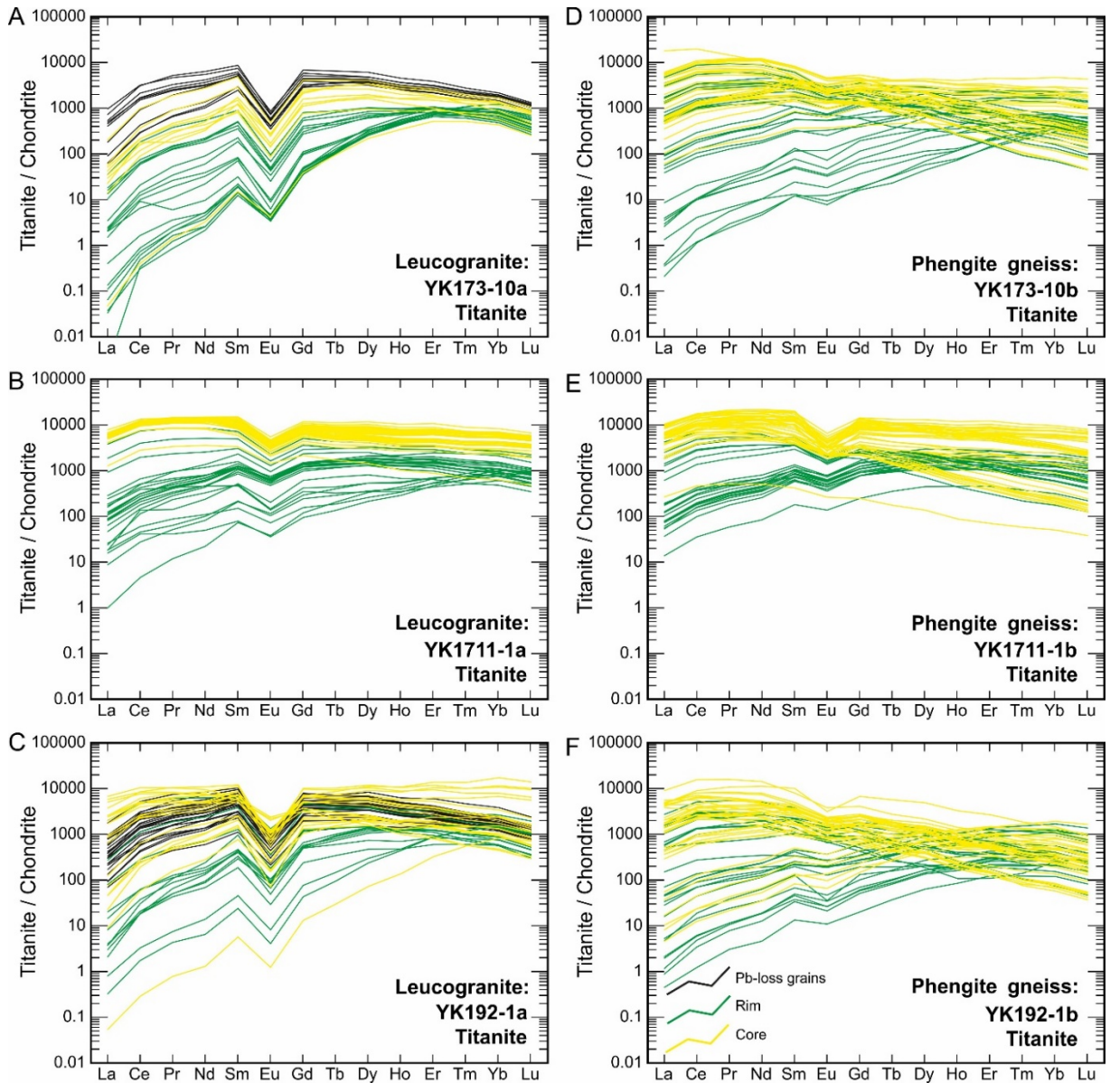

Figure S4. Chondrite-normalized rare earth element patterns for titanite from three leucogranites (A–C) and three phengite gneisses (D–F). Normalizing values are from Sun and McDonough (1989). Line color is related to the petrogenetic interpretation: yellow = core (magmatic); green = rim (metamorphic); black = core or rim with high U/Pb ratios, interpreted to have experienced partial Pb loss.

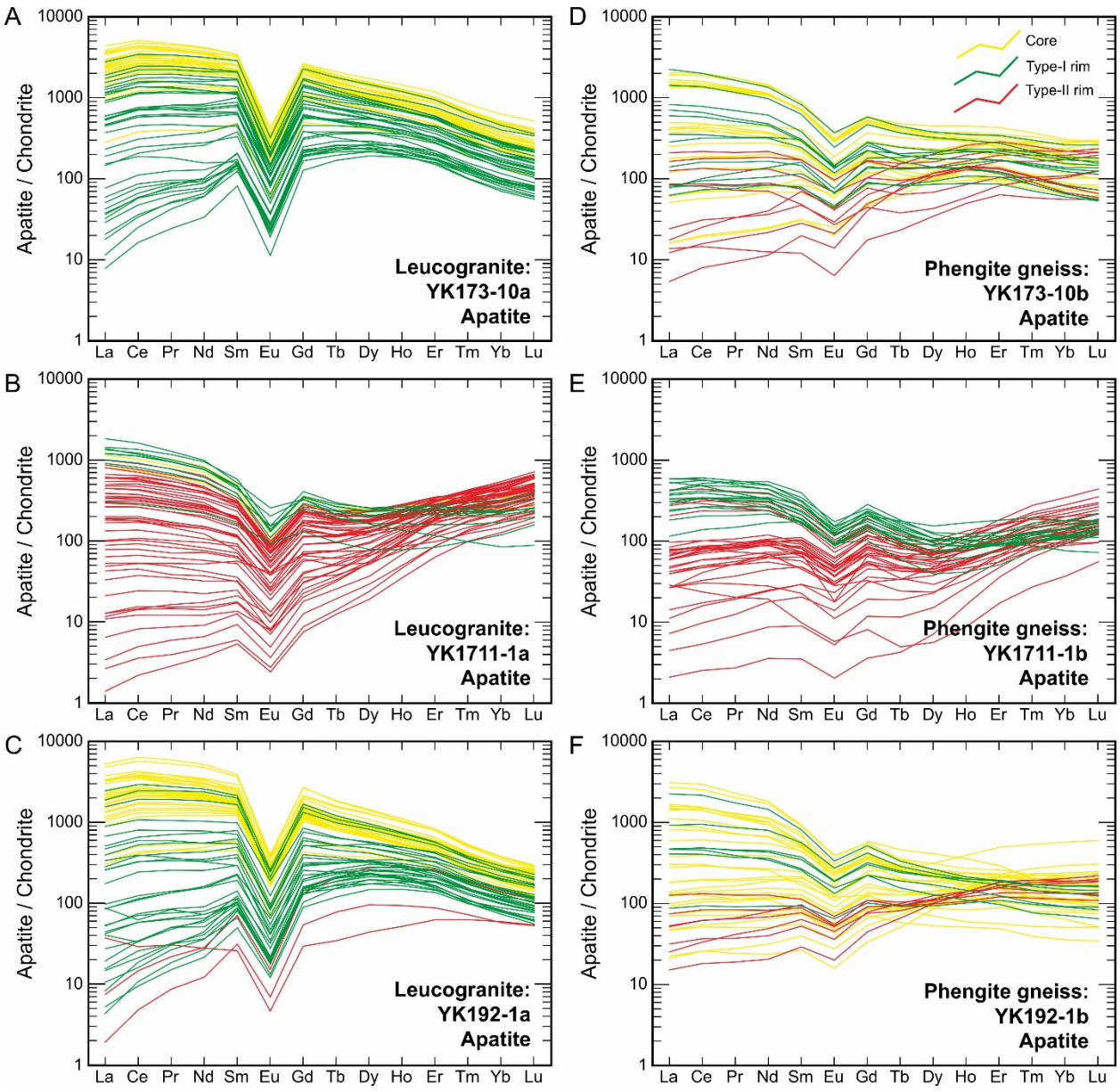

Figure S5. Chondrite-normalized rare earth element patterns for apatite from three leucogranites (A–C) and three phengite gneisses (D–F). Normalizing values are from Sun and McDonough (1989). Line color is related to the petrogenetic interpretation: yellow = core (magmatic), green = Type I rim (metamorphic), red = Type II rim (metamorphic).

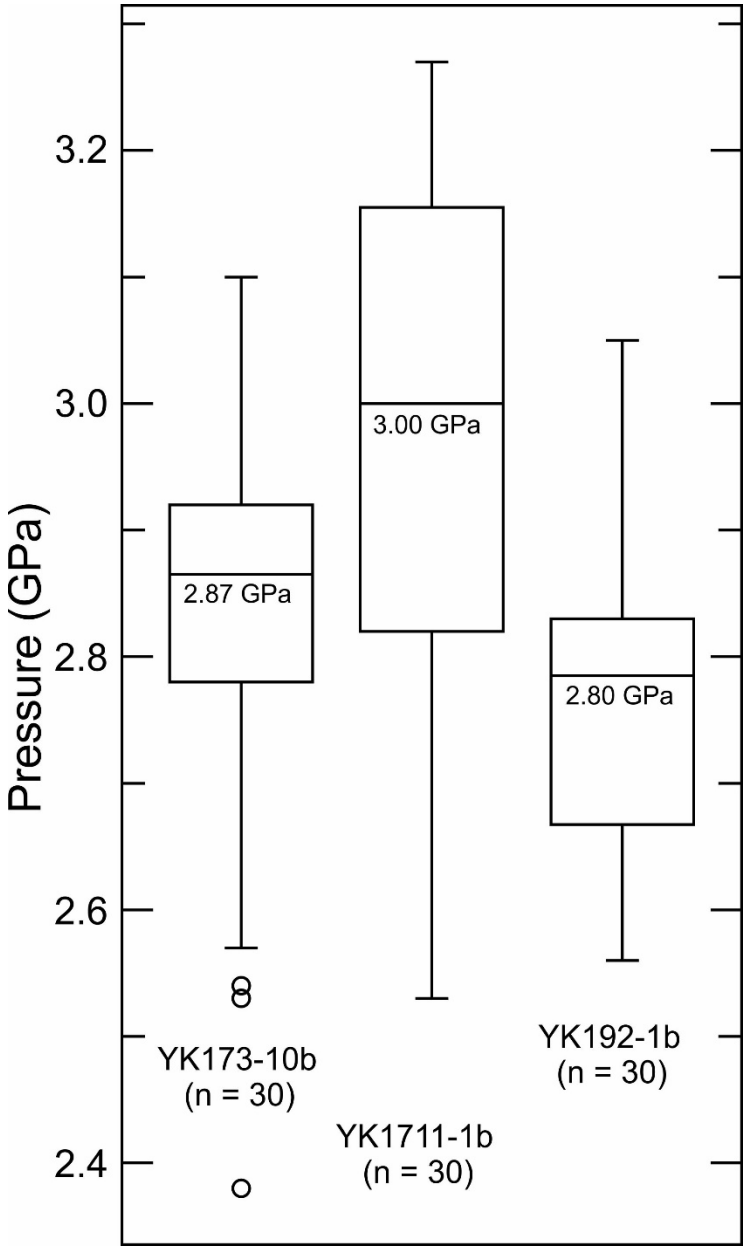

Figure S6. Box-and-whisker plots summarizing pressure for three phengite gneisses calculated at *T* of 800 °C (based on the *P–T–t* path from Xia et al., 2018) using the Si-in-phengite barometer of Caddick and Thompson (2008, equation 8).

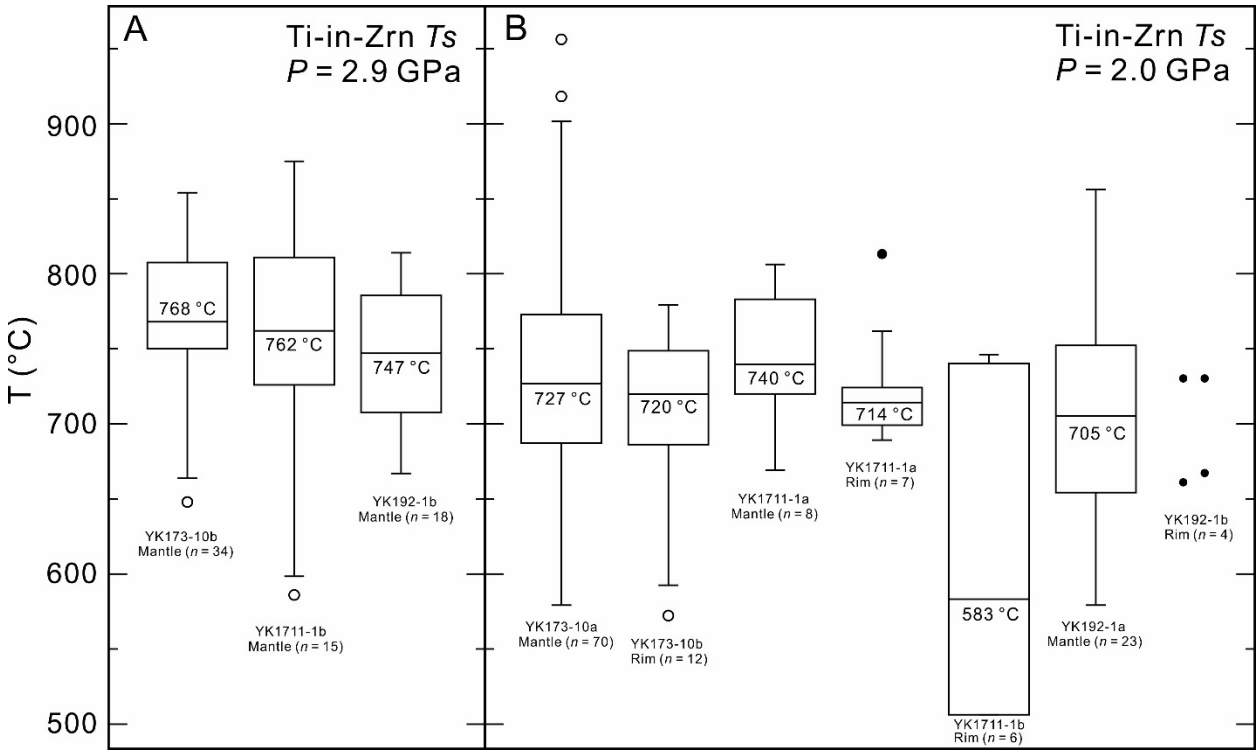

Figure S7. Box-and-whisker plots summarizing temperatures calculated at *P* of 2.9 GPa for mantles of zircon from three phengite gneisses (A) and at a notional *P* of 2.0 GPa for mantles/rims of zircon from three leucogranites and rims of zircon from the phengite gneisses (B). The number of analyses and the median temperature for each sample are shown. The activities of SiO_2 (a_{SiO2}) and TiO_2 (a_{TiO2}) were set as 1.0 and 0.75, respectively (based on the discussion in Ferry and Watson, 2007).

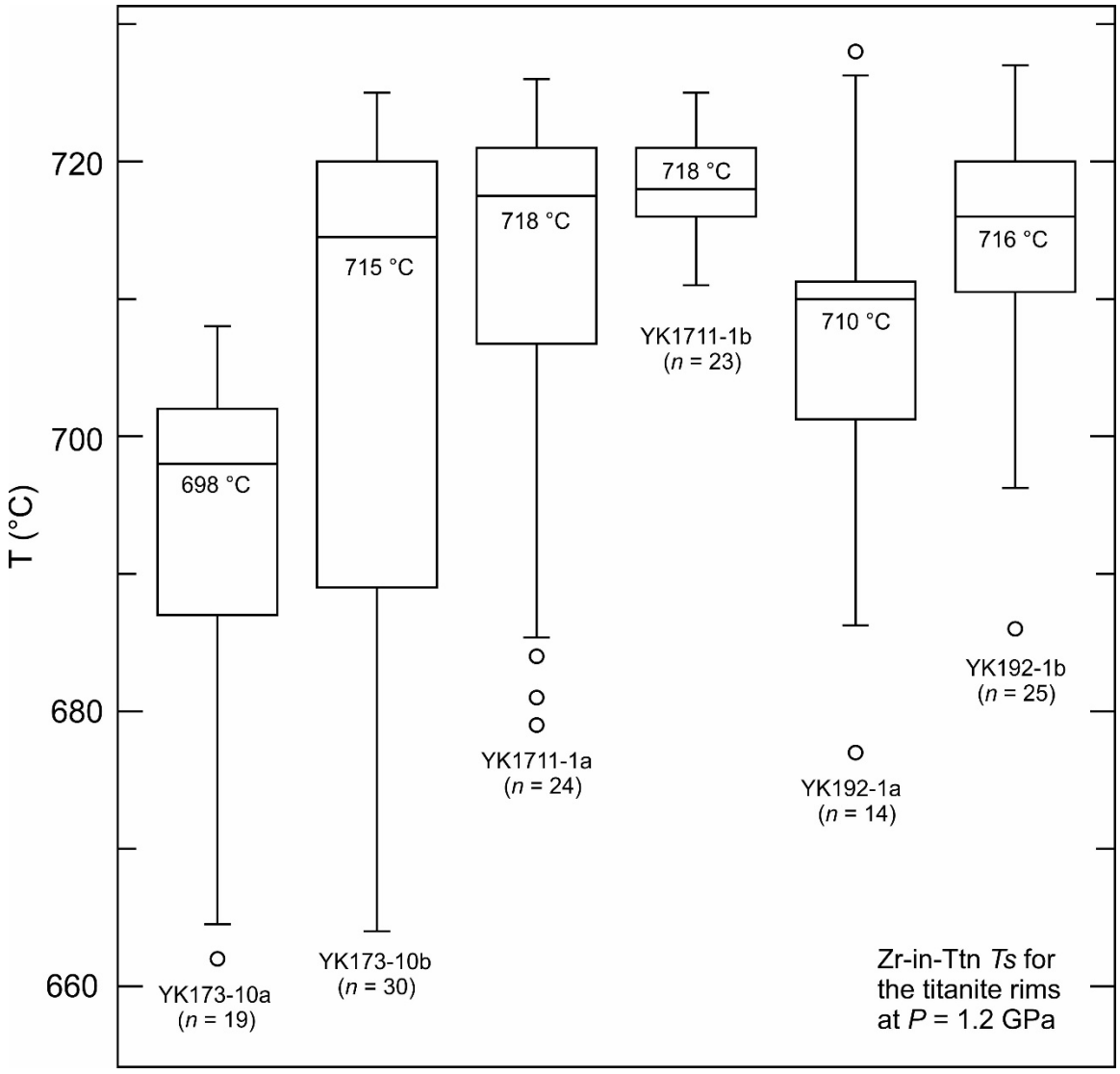

Figure S8. Box-and-whisker plots summarizing temperatures calculated at a notional *P* of 1.2 GPa for rims of titanite from three leucogranites and three phengite gneisses. The number of analyses and the median temperature for each sample are shown. The activities of SiO_2 (a_{SiO2}) and TiO_2 (a_{TiO2}) were set as 1.0 and 0.75, respectively (based on the discussion in both Ferry and Watson, 2007, and Hayden and Watson, 2007).

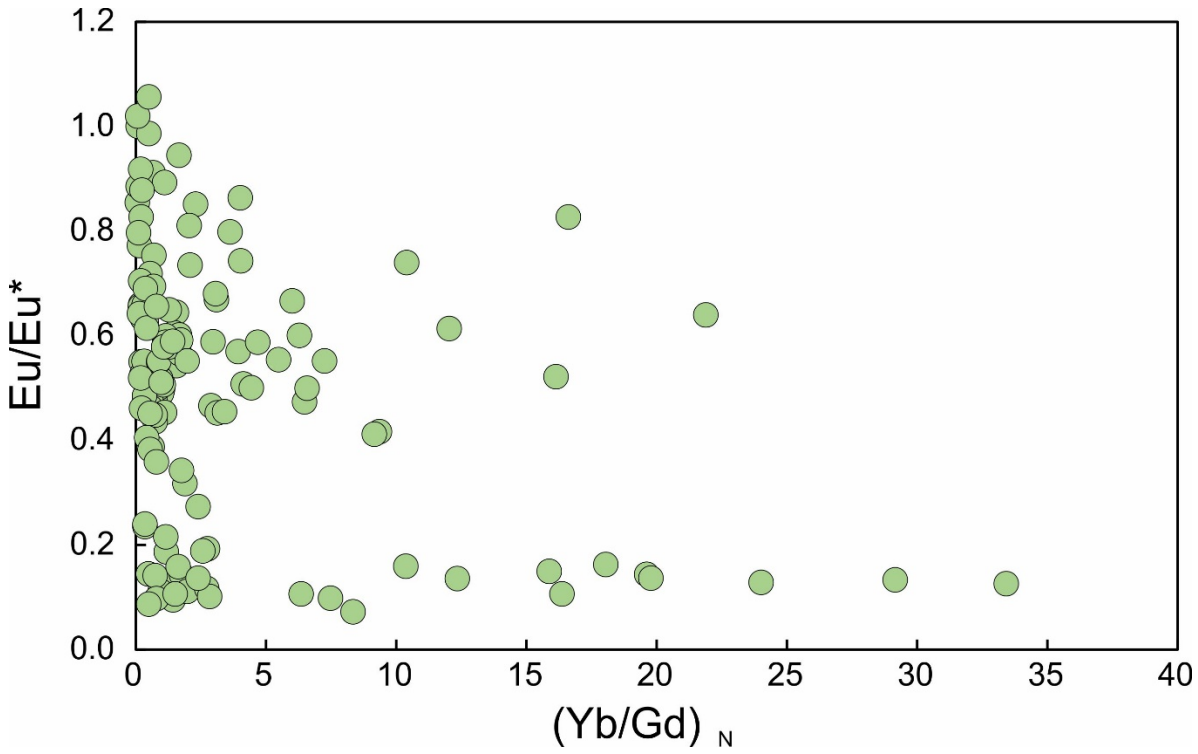

Figure S9. A binary plot of $(Yb/Gd)_N$ vs. Eu/Eu* for rims of titanite from three leucogranites and three phengite gneisses. Normalizing (N) values are from Sun and McDonough (1989).

REFERENCES CITED

Caddick, M.J., and Thompson, A.B., 2008, Quantifying the tectono-metamorphic evolution of pelitic rocks from a wide range of tectonic settings: mineral compositions in equilibrium. Contributions to Mineralogy and Petrology, v. 156, no. 2, p. 177–195, https://doi.org/10.1007/s00410-008-0280-6.

Ferry, J.M., and Watson, E.B., 2007, New thermodynamic models and revised calibrations for the Ti-in-zircon and Zr-in-rutile thermometers. Contributions to Mineralogy and Petrology, v. 154, no. 4, p. 429–437, http://dx.doi.org/10.1007/s00410-007-0201-0.

Hayden, L.A., and Watson, E.B., 2007, Rutile saturation in hydrous siliceous melts and its bearing on Ti-thermometry of quartz and zircon. Earth and Planetary Science Letters, v. 258, no. 3–4, p. 561–568, https://doi.org/10.1016/j.epsl.2007.04.020.

Sun, S.S., and McDonough, W.F., 1989, Chemical and isotopic systematics of oceanic basalts: Implications for mantle composition and processes. Geological Society, London, Special Publications, v. 42, p. 313–345, https://doi.org/10.1144/GSL.SP.1989.042.01.19.

Whitney, D.L., and Evans, B.W., 2010, Abbreviations for names of rock-forming minerals. American Mineralogist, v. 95, no. 1, p. 185–187, https://doi.org/10.2138/am.2010.3371.

Xia, B., Brown, M., Wang, L., Wang, S.J., and Piccoli, P., 2018, Phase equilibria modeling of MT–UHP eclogite: a case study of coesite eclogite at Yangkou, Sulu belt, Eastern China. Journal of Petrology, v. 59, no. 7, p. 1253–1280, https://doi.org/10.1093/petrology/egy060.